

High throughput second harmonic imaging for label-free biological applications

Carlos Macias-Romero,¹ Marie E. P. Didier,¹ Pascal Jourdain,² Pierre Marquet,² Pierre Magistretti,^{2,3} Orly B. Tarun,¹ Vitalijs Zubkovs,¹ Aleksandra Radenovic,⁴ and Sylvie Roke^{1,*}

¹Laboratory for fundamental BioPhotonics, Institute of Bioengineering, École Polytechnique Fédérale de Lausanne (EPFL), 1015, Lausanne, Switzerland

²Laboratory of Neuroenergetics and cellular dynamics, Brain Mind Institute, École Polytechnique Fédérale de Lausanne (EPFL), 1015, Lausanne, Switzerland

³Division of Biological and Environmental sciences and engineering, KAUST, Thuwal, Saudi Arabia

⁴Laboratory of Nanoscale Biology, Institute of Bioengineering, École Polytechnique Fédérale de Lausanne (EPFL), 1015, Lausanne, Switzerland

*sylvie.roke@epfl.ch

Abstract: Second harmonic generation (SHG) is inherently sensitive to the absence of spatial centrosymmetry, which can render it intrinsically sensitive to interfacial processes, chemical changes and electrochemical responses. Here, we seek to improve the imaging throughput of SHG microscopy by using a wide-field imaging scheme in combination with a medium-range repetition rate amplified near infrared femtosecond laser source and gated detection. The imaging throughput of this configuration is tested by measuring the optical image contrast for different image acquisition times of BaTiO₃ nanoparticles in two different wide-field setups and one commercial point-scanning configuration. We find that the second harmonic imaging throughput is improved by 2-3 orders of magnitude compared to point-scan imaging. Capitalizing on this result, we perform low fluence imaging of (parts of) living mammalian neurons in culture.

©2014 Optical Society of America

OCIS codes: (180.4315) Nonlinear microscopy; (170.3880) Medical and biological imaging; (120.4640) Optical instruments; (220.4830) Systems design.

References and links

1. R. Hellwarth and P. Christensen, "Nonlinear optical microscopic examination of structure in polycrystalline ZnSe," *Opt. Commun.* **12**(3), 318–322 (1974).
2. C. J. R. Sheppard, J. N. Gannaway, R. Kompfner, and D. Walsh, "Scanning harmonic optical microscope," *IEEE J. Quantum Electron.* **13**, 912 (1977).
3. I. Freund, M. Deutsch, and A. Sprecher, "Connective tissue polarity. Optical second-harmonic microscopy, crossed-beam summation, and small-angle scattering in rat-tail tendon," *Biophys. J.* **50**(4), 693–712 (1986).
4. B. Masters, *Handbook of Biomedical Nonlinear Optical Microscopy* (Oxford University Press, 2008).
5. W. Denk, J. H. Strickler, and W. W. Webb, "Two-photon laser scanning fluorescence microscopy," *Science* **248**(4951), 73–76 (1990).
6. M. Flörsheimer, R. Paschotta, U. Kubitscheck, C. Brillert, D. Hofmann, L. Heuer, G. Schreiber, C. Verbeek, W. Sohler, and H. Fuchs, "Second-harmonic imaging of ferroelectric domains in LiNbO₃ with micron resolution in lateral and axial directions," *Appl. Phys. B* **67**(5), 593–599 (1998).
7. M. Flörsheimer, M. Bosch, C. Brillert, M. Wierschem, and H. Fuchs, "Second-harmonic imaging of surface order and symmetry," *Thin Solid Films* **327–329**, 241–246 (1998).
8. M. A. Kriech and J. C. Conboy, "Imaging chirality with surface second harmonic generation microscopy," *J. Am. Chem. Soc.* **127**(9), 2834–2835 (2005).
9. T. T. Nguyen and J. C. Conboy, "High-throughput screening of drug-lipid membrane interactions via counter-propagating second harmonic generation imaging," *Anal. Chem.* **83**(15), 5979–5988 (2011).
10. M. A. Kriech and J. C. Conboy, "Counterpropagating second-harmonic generation: a new technique for the investigation of molecular chirality at surfaces," *J. Opt. Soc. Am. B* **21**(5), 1013–1022 (2004).
11. M. D. Peterson, P. L. Hayes, I. S. Martinez, L. C. Cass, J. L. Achtyl, E. A. Weiss, and F. M. Geiger, "Second harmonic generation imaging with a kHz amplifier [Invited]," *Opt. Mater. Express* **1**(1), 57 (2011).

12. E. J. Gualtieri, F. Guo, D. J. Kissick, J. Jose, R. J. Kuhn, W. Jiang, and G. J. Simpson, "Detection of membrane protein two-dimensional crystals in living cells," *Biophys. J.* **100**(1), 207–214 (2011).
13. E. L. DeWalt, V. J. Begue, J. A. Ronau, S. Z. Sullivan, C. Das, and G. J. Simpson, "Polarization-resolved second-harmonic generation microscopy as a method to visualize protein-crystal domains," *Act. Cryst. D* **69**, 74–81 (2013).
14. R. D. Wampler, D. J. Kissick, C. J. Dehen, E. J. Gualtieri, J. L. Grey, H. F. Wang, D. H. Thompson, J. X. Cheng, and G. J. Simpson, "Selective detection of protein crystals by second harmonic microscopy," *J. Am. Chem. Soc.* **130**(43), 14076–14077 (2008).
15. L. Moreaux, O. Sandre, and J. Mertz, "Membrane imaging by second-harmonic generation microscopy," *J. Opt. Soc. Am. B* **17**(10), 1685–1694 (2000).
16. P. J. Campagnola, M. D. Wei, A. Lewis, and L. M. Loew, "High-resolution nonlinear optical imaging of live cells by second harmonic generation," *Biophys. J.* **77**(6), 3341–3349 (1999).
17. H. A. Clark, P. J. Campagnola, J. P. Wuskell, A. Lewis, and L. M. Loew, "Second harmonic generation properties of fluorescent polymer-encapsulated gold nanoparticles," *J. Am. Chem. Soc.* **122**(41), 10234–10235 (2000).
18. P. J. Campagnola, A. C. Millard, M. Terasaki, P. E. Hoppe, C. J. Malone, and W. A. Mohler, "Three-dimensional high-resolution second-harmonic generation imaging of endogenous structural proteins in biological tissues," *Biophys. J.* **82**(1), 493–508 (2002).
19. R. M. Brown, Jr., A. C. Millard, and P. J. Campagnola, "Macromolecular structure of cellulose studied by second-harmonic generation imaging microscopy," *Opt. Lett.* **28**(22), 2207–2209 (2003).
20. P. J. Campagnola, A. C. Millard, M. Terasaki, P. E. Hoppe, C. J. Malone, and W. A. Mohler, "Three-dimensional high-resolution second-harmonic generation imaging of endogenous structural proteins in biological tissues," *Biophys. J.* **82**(1), 493–508 (2002).
21. P. J. Campagnola and L. M. Loew, "Second-harmonic imaging microscopy for visualizing biomolecular arrays in cells, tissues and organisms," *Nat. Biotechnol.* **21**(11), 1356–1360 (2003).
22. S. V. Plotnikov, A. C. Millard, P. J. Campagnola, and W. A. Mohler, "Characterization of the myosin-based source for second-harmonic generation from muscle sarcomeres," *Biophys. J.* **90**(2), 693–703 (2006).
23. D. A. Dombeck, K. A. Kasischke, H. D. Vishwasrao, M. Ingelsson, B. T. Hyman, and W. W. Webb, "Uniform polarity microtubule assemblies imaged in native brain tissue by second-harmonic generation microscopy," *Proc. Natl. Acad. Sci. U.S.A.* **100**(12), 7081–7086 (2003).
24. A. C. Kwan, D. A. Dombeck, and W. W. Webb, "Polarized microtubule arrays in apical dendrites and axons," *Proc. Natl. Acad. Sci. U.S.A.* **105**(32), 11370–11375 (2008).
25. A. C. Kwan, K. Duff, G. K. Gouras, and W. W. Webb, "Optical visualization of Alzheimer's pathology via multiphoton-excited intrinsic fluorescence and second harmonic generation," *Opt. Express* **17**(5), 3679–3689 (2009).
26. S. Psilodimitrakopoulos, V. Petegnief, N. de Vera, O. Hernandez, D. Artigas, A. M. Planas, and P. Loza-Alvarez, "Quantitative imaging of microtubule alteration as an early marker of axonal degeneration after ischemia in neurons," *Biophys. J.* **104**(5), 968–975 (2013).
27. E. Brown, T. McKee, E. diTomaso, A. Pluen, B. Seed, Y. Boucher, and R. K. Jain, "Dynamic imaging of collagen and its modulation in tumors in vivo using second-harmonic generation," *Nat. Med.* **9**(6), 796–801 (2003).
28. P. J. Campagnola and C. Y. Dong, "Second harmonic generation microscopy: principles and applications to disease diagnosis," *Laser Photon. Rev.* **5**(1), 13–26 (2011).
29. J. L. Suhailim, C. Y. Chung, M. B. Lilledahl, R. S. Lim, M. Levi, B. J. Tromberg, and E. O. Potma, "Characterization of cholesterol crystals in atherosclerotic plaques using stimulated raman scattering and second-harmonic generation microscopy," *Biophys. J.* **102**(8), 1988–1995 (2012).
30. G. Latour, I. Gusachenko, L. Kowalczyk, I. Lamarre, and M. C. Schanne-Klein, "In vivo structural imaging of the cornea by polarization-resolved second harmonic microscopy," *Biomed. Opt. Express* **3**(1), 1–15 (2012).
31. G. Latour, L. Kowalczyk, M. Savoldelli, J. L. Bourges, K. Plamann, F. Behar-Cohen, and M. C. Schanne-Klein, "Hyperglycemia-induced abnormalities in rat and human corneas: The potential of second harmonic generation microscopy," *PLoS ONE* **7**(11), e48388 (2012).
32. D. A. Dombeck, M. Blanchard-Desce, and W. W. Webb, "Optical recording of action potentials with second-harmonic generation microscopy," *J. Neurosci.* **24**(4), 999–1003 (2004).
33. L. Sacconi, D. A. Dombeck, and W. W. Webb, "Overcoming photodamage in second-harmonic generation microscopy: real-time optical recording of neuronal action potentials," *Proc. Natl. Acad. Sci. U.S.A.* **103**(9), 3124–3129 (2006).
34. B. A. Nemet, V. Nikolenko, and R. Yuste, "Second harmonic imaging of membrane potential of neurons with retinal," *J. Biomed. Opt.* **9**(5), 873–881 (2004).
35. M. Nuriya, J. Jiang, B. Nemet, K. B. Eisenthal, and R. Yuste, "Imaging membrane potential in dendritic spines," *Proc. Natl. Acad. Sci. U.S.A.* **103**(3), 786–790 (2006).
36. J. Jiang, K. B. Eisenthal, and R. Yuste, "Second harmonic generation in neurons: electro-optic mechanism of membrane potential sensitivity," *Biophys. J.* **93**(5), L26–L28 (2007).
37. D. S. Peterka, H. Takahashi, and R. Yuste, "Imaging voltage in neurons," *Neuron* **69**(1), 9–21 (2011).
38. R. Araya, K. B. Eisenthal, and R. Yuste, "Dendritic spines linearize the summation of excitatory potentials," *Proc. Natl. Acad. Sci. U.S.A.* **103**, 18779–18804 (2006).

39. C. L. Hsieh, Y. Pu, R. Grange, and D. Psaltis, "Second harmonic generation from nanocrystals under linearly and circularly polarized excitations," *Opt. Express* **18**(11), 11917–11932 (2010).
40. P. Pantazis, J. Maloney, D. Wu, and S. E. Fraser, "Second harmonic generating (SHG) nanoprobe for in vivo imaging," *Proc. Natl. Acad. Sci. U.S.A.* **107**(33), 14535–14540 (2010).
41. J. Čulić-Viskotski, W. P. Dempsey, S. E. Fraser, and P. Pantazis, "Surface functionalization of barium titanate SHG nanoprobe for in vivo imaging in zebrafish," *Nat. Protoc.* **7**(9), 1618–1633 (2012).
42. W. P. Dempsey, S. E. Fraser, and P. Pantazis, "SHG nanoprobe: Advancing harmonic imaging in biology," *Bioessays* **34**(5), 351–360 (2012).
43. P. Pantazis, Y. Pu, D. Psaltis, and S. Fraser, "Second harmonic generating (SHG) nanoprobe: A new tool for biomedical imaging," *Proc. SPIE* **7183**, 71831P (2009).
44. R. Grange, T. Lanvin, C. L. Hsieh, Y. Pu, and D. Psaltis, "Imaging with second-harmonic radiation probes in living tissue," *Biomed. Opt. Express* **2**(9), 2532–2539 (2011).
45. P. T. C. So, E. Y. S. Yew, and C. Rowlands, "High-throughput nonlinear optical microscopy," *Biophys. J.* **105**(12), 2641–2654 (2013).
46. E. E. Hoover and J. A. Squier, "Advances in multiphoton microscopy technology," *Nat. Photonics* **7**(2), 93–101 (2013).
47. K. H. Kim, C. Buehler, and P. T. C. So, "High-speed, two-photon scanning microscope," *Appl. Opt.* **38**(28), 6004–6009 (1999).
48. V. Iyer, T. M. Hoogland, and P. Saggau, "Fast functional imaging of single neurons using random-access multiphoton (RAMP) microscopy," *J. Neurophysiol.* **95**(1), 535–545 (2005).
49. K. L. Sly, T. T. Nguyen, and J. C. Conboy, "Lens-less surface second harmonic imaging," *Opt. Express* **20**(20), 21953–21967 (2012).
50. Y. Pu, M. Centurion, and D. Psaltis, "Harmonic holography: a new holographic principle," *Appl. Opt.* **47**(4), A103–A110 (2008).
51. O. Mashizadeh, P. Schlup, and R. A. Bartels, "Label-free second harmonic generation holographic microscopy of biological specimens," *Opt. Express* **18**(10), 9840–9851 (2010).
52. J. Bewersdorff, R. Pick, and S. W. Hell, "Multifocal multiphoton microscopy," *Opt. Lett.* **23**(9), 655–657 (1998).
53. K. Bahlmann, P. T. C. So, M. Kirber, R. Reich, B. Kosicki, W. McGonagle, and K. Bellve, "Multifocal multiphoton microscopy (MMM) at a frame rate beyond 600 Hz," *Opt. Express* **15**(17), 10991–10998 (2007).
54. G. Zhu, J. van Howe, M. Durst, W. Zipfel, and C. Xu, "Simultaneous spatial and temporal focusing of femtosecond pulses," *Opt. Express* **13**(6), 2153–2159 (2005).
55. D. Oron, E. Tal, and Y. Silberberg, "Scanningless depth-resolved microscopy," *Opt. Express* **13**(5), 1468–1476 (2005).
56. A. Vaziri and C. V. Shank, "Ultrafast widefield optical sectioning microscopy by multifocal temporal focusing," *Opt. Express* **18**(19), 19645–19655 (2010).
57. L.-C. Cheng, C.-Y. Chang, C.-Y. Lin, K.-C. Cho, W.-C. Yen, N.-S. Chang, C. Xu, C. Y. Dong, and S.-J. Chen, "Spatiotemporal focusing-based widefield multiphoton microscopy for fast optical sectioning," *Opt. Express* **20**(8), 8939–8948 (2012).
58. H. Choi, E. Y. S. Yew, B. Hallacoglu, S. Fantini, C. J. R. Sheppard, and P. T. C. So, "Improvement of axial resolution and contrast in temporally focused widefield two-photon microscopy with structured light illumination," *Biomed. Opt. Express* **4**(7), 995–1005 (2013).
59. N. Gomopoulos, C. Luetgebaucks, Q. Sun, C. Macias-Romero, and S. Roke, "Label-free second harmonic and hyper Rayleigh scattering with high efficiency," *Opt. Exp.* **21**, 815–821 (2013).
60. J. I. Dadap, X. F. F. Hu, N. M. Russell, J. G. G. Ekerdt, J. K. K. Lowell, M. C. C. Downer, M. Russell, and S. Member, "Analysis of second-harmonic generation by unamplified, high-repetition-rate, ultrashort laser pulses at Si(001) interfaces," *IEEE J. Quantum Electron.* **1**, 1145–1155 (1995).
61. S. Roke, M. Bonn, and A. V. Petukhov, "Nonlinear optical scattering: The concept of the effective susceptibility," *Phys. Rev. B* **70**(11), 115106 (2004).
62. R. Le Harzic, I. Riemann, K. König, C. Wüllner, and C. Donitzky, "Influence of femtosecond laser pulse irradiation on the viability of cells at 1035, 517, and 345," *J. Appl. Phys.* **102**(11), 114701 (2007).
63. A. Vogel, N. Linz, S. Freidank, and G. Paltauf, "Femtosecond-laser-induced nanocavitation in water: implications for optical breakdown threshold and cell surgery," *Phys. Rev. Lett.* **100**(3), 038102 (2008).
64. K. König, "Multiphoton microscopy in life sciences," *J. Microsc.* **200**(2), 83–104 (2000).
65. C. Macias-Romero, M. E. P. Didier, L. Delannoy, F. Dutto, A. Radenovic, and S. Roke, "Probing rotational and translational diffusion of nanodiamonds in living cells on microsecond time scales," *Nano Lett.* **14**, 2552–2557 (2014).
66. L. R. Squire, F. E. Bloom, N. C. Spitzer, S. Du Lac, A. Gosh, and D. Berg, *Fundamental Neuroscience* (Elsevier, 2008).
67. O. D. Therrien, B. Aubé, S. Pagès, P. D. Koninck, and D. Côté, "Wide-field multiphoton imaging of cellular dynamics in thick tissue by temporal focusing and patterned illumination," *Biomed. Opt. Express* **2**(3), 696–704 (2011).

Introduction

Second-harmonic generation (SHG) is an elastic two-photon process in which two photons are transformed by a material into one photon with the double frequency. SHG is inherently sensitive to the presence of spatial non-centrosymmetry. Therefore it is sensitive to bulk non-centrosymmetric structural spatial arrangements (in fibrils or in crystals), interfaces, or electric field induced breaking of symmetry. SHG imaging was demonstrated in the 1970's [1,2] and was first applied to imaging tissues in the 1980's [3]. Thanks to the development of, among other things, ultrafast laser sources, it is only in the two recent decades that SHG imaging has seen a tremendous development [4,5]. SHG imaging has been applied in many chemical, biological and medical applications. For example, ferroelectric domains in niobate crystals [6], dye covered Langmuir films [7] modified membranes [8–10] (using the UV resonance of biomolecules), quantum dots [11], and non-centrosymmetric crystal structures of proteins at very low concentrations in solution and bacteria have been successfully explored [12–14].

The intrinsic energy conservation of the SHG process ensures low photo-damage and -toxicity, which is ideal for imaging of biological and medical samples. SHG imaging has been used to visualize the membrane of vesicles [15] and cell membranes with the aid of fluorophore labeling [16,17], and to image tissues that are rich in endogenous non-centrosymmetric material, such as collagen [18–20], muscle myosin [21,22] and microtubulin fibrils [23–26]. The latter has been used to determine the microtubule organization in neurons [23,24]. SHG studies have also been performed to aid medical diagnostic purposes [25–29] and medicine development [30,31]. Voltage sensitive membrane specific markers have permitted for single site time dependent optical recordings of membrane potential activity [32–37]. This enabled the team of Yuste and Eiselthaler to measure the length of the dendritic spine necks in living neurons and to determine that dendritic spines linearize the summation of excitatory potentials [38]. In another promising approach, SHG active surface modifiable non-centrosymmetric nanodoublers [39] have been introduced as a practical alternative to fluorescent molecules and quantum dots, to track processes through in-vitro (cell) imaging [40–44]. These studies clearly demonstrate the unique ability and promising possibilities of SHG microscopy to probe materials and interfaces, identify and quantify histoarchitectural tissue alterations, and to track changes in living systems.

Even though SHG imaging is used in a wide range of applications, the imaging throughput, defined as number of detected photons per frame per second, is still relatively low compared to linear microscopy [45]. An improvement of the imaging throughput could enable the use of SHG imaging to detect dynamical biological processes that occur on the (sub) millisecond time scale, or advance the use of label-free SHG imaging for material studies or clinical applications. Label-free imaging applications are of interest for clinical and long-term measurements; labels (chromophores or particles) inevitably interfere with the process of interest and are often toxic, limiting the imaging time significantly. Two approaches are taken to improve imaging throughput (reviewed in [45,46]): The first one is to improve the scanning speed of the microscope in combination with the use of faster repetition rate laser sources [47,48]. The second one is to parallelize the imaging process. Recent advancements [46] include wide-field counter propagating SHG geometries [10,11], lens-less imaging approaches [49], harmonic holography [50,51], multi-confocal imaging [52,53], and spatiotemporal wide-field illumination [54–58].

Recently we presented a method to perform high throughput SHG scattering experiments to obtain elastic non-resonant surface responses from unlabeled 80 nm sized liposome membranes in aqueous solution with 5 millisecond acquisition times, in which we employed a medium-ranged (200 kHz) repetition rate femtosecond amplified laser system in combination with gated detection [59]. In principle this throughput could also be achieved in an imaging application. We therefore investigate here the possibilities of SHG imaging using a wide-field

illumination scheme in combination with such a laser source and gated detection. We start by considering the parameters that are needed to maximize imaging throughput, so that laser fluences can be kept low (as required for biological imaging), and characterize the optical parameters of our proposed scheme. Then, we compare our approach to a commercial scanning SHG microscope, and a previously published wide-field approach employing a 1 kHz near infrared femtosecond laser as light source. We find an improvement in imaging throughput of 2-4 orders of magnitude compared to the commercial scanning system and the 1 kHz system. Finally, we explore the possibilities for label-free low fluence imaging of single living neurons in culture.

Imaging throughput considerations

To maximize the imaging throughput, defined as number of detected photons per image per second, of an SHG imaging system, we consider the number of photons N_i produced per second per illuminated area [60]:

$$N_i \propto |\Gamma^{(2)}|^2 \frac{E_{p,i}^2}{\tau_i A_i} f_i, \quad (1)$$

where $\Gamma^{(2)}$ is the effective second-order surface susceptibility of the probed (curved) surface or microscopic object [61], $E_{p,i}$ is the pulse energy (in J), with pulse duration τ_i in s, illumination area A_i , (in m^2) and repetition rate f_i (in Hz). The subscript i refers to the two different configurations considered here: wide-field (wf) and scanning (s). It is clear from Eq. (1) that decreasing the area and increasing the repetition rate increases N_i . However, to calculate the throughput in an imaging system it is necessary to take into account the ratio between the size of the image and the illumination area. We therefore assume that for the scanning system the scanning rate is one image frame per second, and that this image is formed by $n = A_{wf}/A_s$ scanning points. The latter is a reasonable assumption, but somewhat on the low side as it is common in scanning systems to oversample the image. Assuming that the pulse wavelength, duration, and fluence ($F_i = E_{p,i}/A_i$) is equal for both scanning and wide-field systems, we have $\tau_{wf} = \tau_s$, and $E_{wf} = E_s n$. We can then compute the throughput ratio N_{wf}/N_s as

$$\frac{N_{wf}}{N_s} = n \frac{f_{wf}}{f_s}. \quad (2)$$

Thus for an image with 100 x 100 (or 1000 x 1000) scanning points and a repetition rate $f_s = 100$ MHz, a wide-field system delivers more photons per image per second if $f_{wf} > 10$ (or 0.1) kHz. A further significant improvement is possible with higher repetition rates: A 100 kHz system may reach a 10 - to 1000-fold improvement depending on the image size. This is indeed what is observed in Fig. 1(a) when plotting the imaging throughput as a function of fluence for three different imaging schemes: a scanning system (80 MHz, 820 nm, 190 fs) with an illumination diameter of 0.5 μm , image size of 100 x 100 μm (black line, comparable to e.g [40]. or [23]); a wide-field double-beam illumination (1 kHz, 800 nm, 120 fs) with an illumination ellipse with diameters of 250 and 1000 μm (emission area with a diameter of 250 μm , green line, e.g [11].); and a wide-field double-beam illumination representative of the setup used in this work (200 kHz, 1028 nm, 190 fs) with an illumination ellipse with diameters of 100 and 140 μm (emission area with a diameter of 85 μm , red line). The relative imaging throughput of the red line is larger than the other two. As a consequence of the increased imaging throughput, lower laser fluences can be used.

Low fluence imaging is of particular importance in biological imaging. Irrespective of the mechanism to induce damage, imaging of living specimens requires that the delivered energy per area be kept as low as possible, so that the cells are minimally perturbed by the laser pulses. It has been reported that unstained CHO cells slow their growth rate and die above

fluences of 381 and 1222 mJ/cm², respectively [62], when illuminating with 1035 nm wavelength, 393 fs pulses, 100 kHz repetition rate, and 10 x 50 μs dwell time. Figure 1(b) shows a calculation of the delivered fluence as a function of delivered laser power for the three different illumination schemes used in the calculation of Fig. 1(a). Damage thresholds are indicated by the colored area in Fig. 1(b). Larger illumination areas allow for lower fluences, and in the case of the wide-field configuration the used fluences are well below the reported damage thresholds. Figure 1(c) displays the equivalent average intensities for comparison.

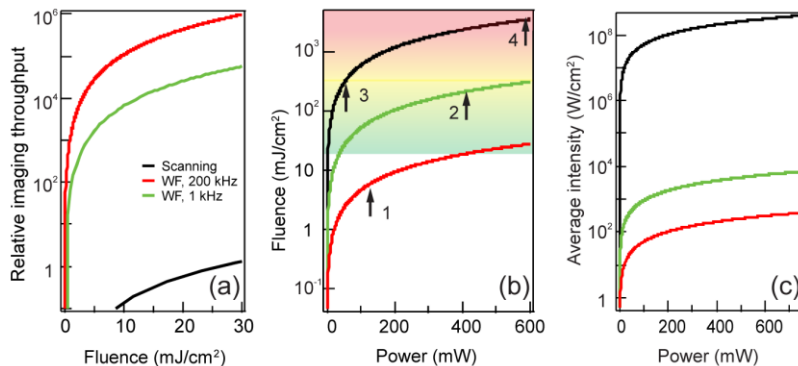


Fig. 1. Calculated imaging throughput. (a) The imaging throughput for a given fluence (proportional to the number of emitted photons per image) for a scanning imaging system (black line), a wide-field imaging system as described here (red line), and a 1 kHz wide-field system (green line). (b) Calculation of the delivered fluence for a given power for the three different systems; the illumination parameters can be found in the text. The arrows in (b) indicate the upper limits quoted in different works: 1 – This work; 2 – in [11]; 3 – in [40] and 4 – in [23] (4). The colored area illustrates for which fluences unstained CHO cells start to be perturbed in growth (yellow) and permanently damaged (red) [62]. (c) For comparison, the corresponding delivered average intensities.

It should be noted, however, that in reality the fluence for a scanning system is lower than the numbers used here since each pixel has a dwell time that is usually less than a millisecond. How much this matters for the actual damage done to a system depends on the optical transition, the excited state, and the energy transfer and transport equations that govern the phototoxicity and damage process. It is also likely that a certain spot on the sample may receive photons from neighboring scanning points so that it is not trivial to quantify these effects. For low repetition rates, effects such as white light generation become important. In terms of achieving maximum imaging throughput with our approach, it is thus likely that the energy transport mechanisms play an important role, which suggests that the maximum gain in imaging throughput is reached for repetition rates of ~1 MHz [63,64].

Imaging system and characterization

Based on the imaging throughput considerations, we employ two weakly focused counter propagating beams as in [10,11] with an additional prism for efficient coupling (see Fig. 2(a)). Compared to the systems of [10,11] the illumination source and detector is very different. Kriech and Conboy in [10] used unfocused light from an optical parametric oscillator with a repetition rate of 10 Hz and pulse duration of 7 ns and 10 mJ output per pulse centered at 550 nm wavelength; the beam had a diameter of 2 mm incident on the sample at an angle of 70°, and the detection consisted of a monochromator followed by a photomultiplier tube. Peterson et al in [11] used 800 nm, 120 fs, 1 kHz laser pulses focused down to an elliptic area of $\pi(125 \times 500 \mu\text{m})^2$ with an unspecified power of 40-400 mW, and a CCD camera for detection. Our light source consists of a Yb:KGW amplified laser (Pharos

Light Conversion), delivering 200 kHz, 1028 nm, 190 fs laser pulses with energies of 0.1 - 0.8 μ J to an elliptical illumination spot size of 100 x 140 μ m in diameter.

More specifically, the light passes through a band pass filter (1028/10 nm, EKSPLA), and is split equally over two counter propagating beams (with a 90° angle) that are coupled into the sample chamber using a 45° prism. Each beam was polarization controlled using zero-order quarter and half wave plates, so that 8 polarization configurations are possible, and focused on the sample with a $f = 20$ cm doublet lens (Thorlabs). The average power at the sample did not exceed 160 mW. The SHG photons were created in a cylindrical volume that is ~ 85 μ m wide and 70 μ m in depth, determined by the pulse duration and angle of incidence of the incoming beams. The sample was imaged by a 50x objective lens (Mitutoyo Plan Apo NIR HR Infinity-Corrected Objective, 0.65 NA) in combination with a tube lens (Mitutoyo MT-L), a 800 nm short pass filter (omega optical), a 515 nm band pass filter (Omega Optical, 10 nm bandwidth) and an EM-ICCD camera (PiMax4, Princeton Instruments). A meniscus lens was placed behind the objective lens to remove spherical aberrations induced by the coverslip. The objective lens has a field of view larger than the illumination area. Figure 2(b) shows a spectrum of the incident beam just before it hits the sample (FWHM ~ 9 nm). Figure 2(c) shows a cross-correlation obtained by delaying the pulses while imaging a single 50 nm BaTiO₃ nanoparticle. The pulse duration at the focus is 197 fs (assuming a Gaussian beam shape). Compared to the original input beam parameters (190 fs, 8.7 nm), there is little change in pulse parameters.

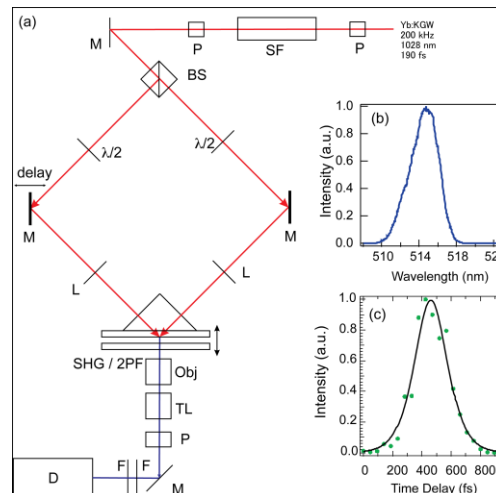


Fig. 2. Optical Layout. (a) The optical layout of the microscope. Symbols: P: polarizer, SF: spatial filter, M: mirror, $\lambda/2$: half wave plate, L: lens, Obj: objective lens, TL: tube lens, F: filter, D: Detector. The sample cell is configured with two glass coverslips in between which a liquid flow can be established. (b) The spectrum of the SHG beam at the sample. (c) The intensity cross-correlation, measured with a single BaTiO₃ nanoparticle in the focus and varying the temporal delay.

Epi-detection can be implemented easily by rearranging the incoming beams, changing the prism to a flat top prism, and correcting for spherical aberrations. In the imaging system of Fig. 2, the illuminating section has a larger depth of field compared to scanning nonlinear microscopes and spatiotemporal focusing microscopes [54–58]. It is possible to limit the illumination depth by e.g. using a 5 micron high sample cell [65] or by producing axial cross-sections using structured illumination [58]. The latter is possible but has not been implemented in the present microscope. In principle spatiotemporal focusing shares some of the improvement in imaging throughput. The detection is different, and spatiotemporal aberrations induced by e.g. biological specimens are no issue here.

Imaging throughput measurements

To test the throughput of this configuration, we have measured SHG images of 50 nm BaTiO₃ nanoparticles that were deposited on a coverslip using fiducial markers. We tested three different illumination conditions, corresponding roughly to the configurations used in the calculation of Fig. 1. We measured images from the same spot on the same sample with the same wavelength and pulse duration. The fluence was 10.5 mJ/cm² for the 1 kHz system or 2.55 mJ/cm² otherwise and the imaging acquisition time was varied. The contrast (amplitude of the signal divided by its spanning range) was calculated for each image and plotted as a function of acquisition time in Fig. 3(a). The black data points were taken with a Leica TCS SP5 scanning microscope in transmission mode, the blue and the red data points were obtained with the SHG wide-field system of Fig. 2 (using different gain settings for the camera), and the green data points were obtained by reducing the repetition rate of our laser to 1 kHz and using a regular CCD camera, i.e. without intensifier or electron multiplier, with a quantum efficiency of 50%. Figure 3(b) shows cross-sections of the images at the position depicted by the blue line in the inset Fig. 3(a), image obtained for the red data points. Figure 3 suggests that the same contrast (or image quality) can be obtained with either one of the systems, but with acquisition times that are 2-3 orders of magnitude shorter when using the wide-field system of Fig. 2.

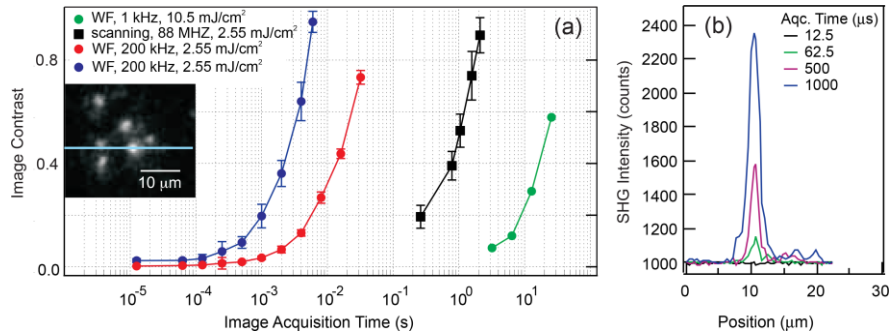


Fig. 3. Measured imaging throughput. (a) Measured contrast in the images recorded from the same position of the same sample in four different systems: wide-field (200 kHz, gated detection as proposed here, blue and red curves), a scanning microscope (Leica TCS SP5 with 1028 nm, 88 MHz, 190 fs laser pulses illumination, a 1.2 NA 20x water immersion objective, a scanning rate of 1000 Hz/line, image size of 256 x 256 pixels, and collecting NA of 0.9), and a wide-field 1 kHz geometry with a normal CCD camera. The used pulse power and repetition rate are given in the legend. The blue data points were recorded with the intensifier and the electronic amplification of the camera both turned on, while the red data points were recorded with only the intensifier on. The inset shows an image of the nanoparticle sample corresponding to the largest red data point. The horizontal blue line indicates the position for which the intensity cross-sections are displayed in (b). (b) Intensity (raw data) versus position for various acquisition times corresponding to the red data points in (a).

An increase in imaging throughput of several orders of magnitude can thus be obtained compared to the 1 kHz configuration (similar to [11]) and the commercial scanning system for elastic SHG imaging. To confirm this conclusion, however, we first verify that our data points are indeed reasonable compared to published literature. Regarding the scanning measurement of the BaTiO₃ nanoparticles, we can make a direct comparison to the work of Pantazis et al. in [40], who imaged immobilized 30 – 90 nm BaTiO₃ nanoparticles in a scanning configuration, using 820 nm, 80 MHz, 300 fs pulses focused down to a $\pi \times (0.26 \mu\text{m})^2$ focal area with a power of 5 mW. They calculated the signal to noise ratio (SNR) of their images to be 10 when imaging at 20 frames/s (or 50 ms/frame) an area of $0.69 \times 0.69 \mu\text{m}^2$ and using a 40 nm-broad bandpass filter. Taking those parameters, their fluence would be $F = 29.4 \text{ mJ/cm}^2$. For our scanning data (black curve), an SNR of 13 is obtained using 50 nm nanoparticles if we scan at 0.48 frames/s (2.1 s/frame) an area of

30x30 μm^2 , with a fluence of 2.55 mJ/cm^2 and using a 50 nm-broad bandpass filter (BP525/50). Comparing the image acquisition time, we have 2.1 s vs 50 ms in [40]. Thus, we have a factor of 42 longer in the acquisition time, but this is obtained with a fluence that is a factor of 11.8 smaller. Correcting for the difference in fluence, scanning areas, pulse durations, frame rate, and SNR, it therefore seems that the imaging throughput of our scanning measurement compares well with that of the literature. Table 1 lists the parameters used and the computation made. Note that the spread in particle size does induce an inaccuracy in the result of the computation. A direct comparison of the green line with Peterson et al in [11] is difficult as the sample is different. In [11], Peterson et al imaged CdSe quantum dots with 600 s image acquisition time. In [40] it is shown that both images of CdSe quantum dots and BaTiO₃ nanoparticles can be compared at an SNR of 10. This means that if we compare our acquisition time per image of 25 s at an SNR of 13 (1 mW, 10.5 mJ/cm^2) with the listed 600 s (20-200 mJ/cm^2), assuming that the SNR in [11] is the same as than in [40], the throughput of our system is similar to [11] (see Table 1). Note that the calculated number is influenced by the difference between SHG and two-photon response of the BaTiO₃ and CdSe [40], respectively, and to the different detection systems. It follows nonetheless that the imaging throughput of the point scanning and 1 kHz wide-field imaging configurations is comparable to the imaging throughput of the homologous configurations used to produce the (scanning) black and the (wide-field) green data points in Fig. 3.

Table 1. Comparison of the measurements in Fig. 3(a) with those of the literature

	Scanning [40]	Scanning, black data in Fig. 3(a)	Wide-field [11]	Wide-field, green data in Fig. 3(a)
SNR	10	13	10	13
Acq. Time	0.05 s	2.1 s	600 s	25 s
Area (Frame)	(0.69 μm) ²	(30 μm) ²	$\pi(125 \mu\text{m})^2$	$\pi(50 \mu\text{m})^2$
Pulse duration	300 fs	190 fs	120 fs	190 fs
Fluence	29.4 mJ/cm^2	2.55 mJ/cm^2	20-200 mJ/cm^2	10.5 mJ/cm^2
	Scanning [40] / black, Fig. 3(a)		Wide-field [11] / green, Fig. 3(a)	
Throughput ratio	$\left(\frac{29.4}{2.5}\right)^2 \left(\frac{10}{13}\right) \left(\frac{0.69}{30}\right)^2 \left(\frac{2.1}{0.05}\right) \left(\frac{190}{300}\right) = 1.1$		$\left(\frac{20}{10.5}\right)^2 \left(\frac{10}{13}\right) \left(\frac{125}{50}\right)^2 \left(\frac{25}{600}\right) \left(\frac{190}{120}\right) = 1.2$	

Thus, the proposed configuration indeed generates an increase in throughput of several orders of magnitude for elastic SHG microscopy over a scanning geometry or a wide-field scheme with low repetition rate. Having developed and characterized an SHG microscope with high throughput, we use it for low fluence label-free imaging of parts of living neurons in culture.

Label-free SHG imaging of sub-cellular structures

Figure 4 shows images of living mammalian neurons in culture (from E17 OF1 mice embryos) placed in a flow chamber. Figure 4(a) shows a sketch of the chamber together with the used polarization combination of the beams. Figure 4(b) shows the bright field image of the cultured neurons. The image displays a neuronal cell body from which arose several dendritic-like processes and probably surrounded by axonal-like beaded fibers. Figure 4(c) shows the emitted spectrum of the neurons under illumination with the 1028 nm pulsed beams. The spectrum consists of a broad bandwidth emission together with a narrow bandwidth signal centered at 514 nm. When the electronic gate of the detector is shifted in time, the narrow band signal vanishes, while the broad emission spectrum can still be detected (albeit with less intensity) under these conditions. Thus, we assign the narrow bandwidth signal to the endogenous SHG response of the neurons, and the broad bandwidth emission to originate from two-photon fluorescence. The image in Fig. 4(d) displays the two-photon emission signal and Fig. 4(e) the second harmonic response of the neurons. Note that the color scale of both images has been inverted to improve contrast, so that dark regions

represent high intensities. Figure 4(f) is a composite image that shows that the source of the two-photon emission (blue) and the second harmonic generation (yellow) are not the same. In Fig. 4(d) we observe elongated grey structures as well as dark bright dots. Comparing the observed structures to previous studies [23,24], we speculate that the elongated grey line structures that exhibit a stronger signal correspond to microtubules which are a main component of the neuronal cytoskeleton involved in cell trafficking and axonal transport [66]. To make more precise and definitive structural assignments, a comparison of these images to images taken with targeted labeling is needed, which is beyond the scope of this work.

Comparing the illumination parameters to literature, the SHG images in Fig. 4 were recorded with 6 s acquisition times, a fluence of 7.3 mJ/cm^2 (or averaged intensity $\langle I \rangle = 147 \text{ W/cm}^2$), and SSS polarization. Compared to earlier work on unstained neuronal cultures by Dombeck et al. [23] who used a 120 s acquisition time and averaged intensities of $\sim 30 \text{ MW/cm}^2$ ($= 3400 \text{ mJ/cm}^2$), the acquisition time and fluence is drastically reduced. Spatiotemporal focusing techniques have not yet been used for label-free imaging of living neurons [67]. Thus, we show here that the increased imaging throughput can be used to reduce the imaging acquisition time and/or the fluence, which results in a significant reduction of photodamage probability.

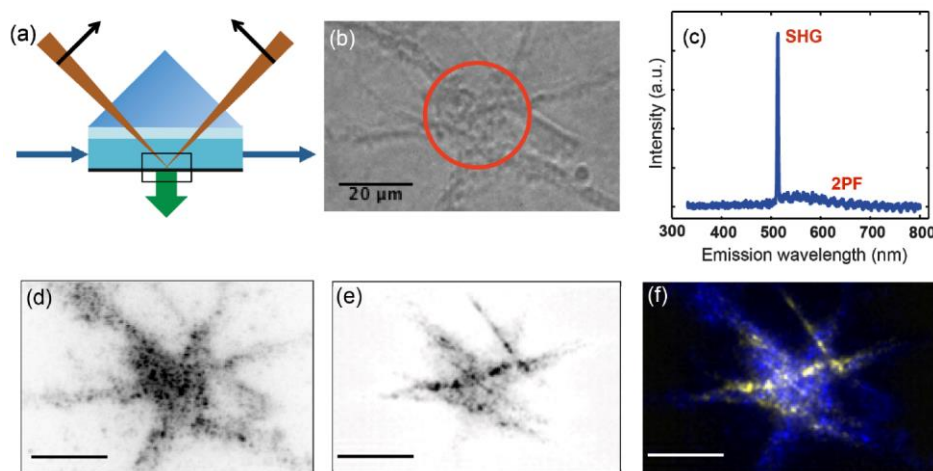


Fig. 4. Label-free SHG imaging of living neurons. (a) Schematic of the flow chamber. The neurons are placed on a glass coverslip (as indicated by the box) under flow of HEPES buffer solution. The polarization configuration of the beams was SSS. (b) A bright field image of a part of the neuronal culture that was subsequently imaged with SHG. The image was obtained by placing a white light source in the beam path of one of the incoming beams. (c) The spectrum of the part of the cell indicated by the red circle in (b), collected by a spectrometer placed before the detector. (d) Inverted image of the endogenous two-photon fluorescence signal. (e) Inverted image of the endogenous SHG signal, obtained by placing a band pass filter (515/BP10) before the camera. Dark regions correspond to high intensities. (f) Composite image of (d) and (e), showing both the fluorescence (blue) and SHG signal (yellow). Images (d) and (e) were obtained with a 6 s acquisition time and a fluence of 7.3 mJ/cm^2 (or averaged intensity $\langle I \rangle = 147 \text{ W/cm}^2$). All images represent living neurons, confirmed after every experiment by monitoring in dark-field physiological changes as induced by a neurotransmitter.

Conclusions

In summary, we have implemented changes in the optical layout of a second harmonic imaging system that increases the second harmonic imaging throughput for label-free elastic SHG imaging by several orders of magnitude. The increase in throughput was achieved with a wide-field geometry and medium repetition rate laser source in combination with gated detection. In addition to enhanced throughput, the pulse duration is not distorted and can be

measured directly at the sample, and dynamic and ultrafast measurements can be performed readily with all 8 possible polarization directions. Label-free second harmonic and two photon fluorescence imaging and spectroscopy of living neurons have been performed with short acquisition time and at very low fluences. Clear second harmonic emission is observed from the neurons, which is emitted from different locations as the two-photon fluorescence.

Acknowledgments

This work was supported by the Julia Jacobi Foundation, the Swiss National Foundation (grant number 200021-146884), and European Commission, Research Executive Agency Marie Curie Actions 'FINON' (ITN-2013-607842). We would like to thank Prof. K. B. Eisenthal for very inspiring discussions.